Dalton Transactions

PAPER

View Article Online
View Journal | View Issue

Cite this: *Dalton Trans.*, 2019, **48**, 15465

Downsizing of robust Fe-triazole@SiO_2 spin-crossover nanoparticles with ultrathin shells†

R. Torres-Cavanillas, [a] L. Lima-Moya, [a] F. D. Tichelaar,[b] H. W. Zandbergen,[b] M. Giménez-Marqués *[a] and E. Coronado *[a]

Received 4th June 2019,
Accepted 20th June 2019

DOI: 10.1039/c9dt02086a

rsc.li/dalton

A chemical protocol to design robust hybrid [Fe(Htrz)$_2$(trz)](BF$_4$)@SiO_2 nanoparticles (NPs) with sizes as small as 28 nm and ultrathin silica shells below 3 nm has been developed. These NPs present a characteristic abrupt spin transition with a subsequent decrease in the width of the thermal hysteresis upon reducing the NP size.

Spin-crossover (SCO) compounds represent a current focus of interest in molecular magnetism owing to their ability to undergo low-spin (LS) to high-spin (HS) transitions under the influence of external stimuli such as temperature, pressure, light or electric field.[1–3] In contrast to the vast majority of magnetic molecular materials, these smart materials often exhibit the spin transition near room temperature. Such a feature makes them appealing for the design of switchable devices for information processing.[4] In this context, the 1D triazole-based Fe^{II} coordination polymers of general formula $[Fe(Rtrz)_3]X_2$ [5] (Rtrz = 4-R-1,2,4-triazole and X = monovalent anion) are generally considered the most promising SCO materials, since they exhibit a large thermal hysteresis near room temperature.[6]

A significant advance in this field was the miniaturization of these SCO materials in the form of nanoparticles (NPs),[7–14] promoting their use as active elements in nanoelectronic memory devices with spin-state switching functionality.[15–20] Albeit the studied SCO devices have contributed to bridge the existing gap for real application several drawbacks still need to be solved. In particular, most of the SCO-based devices confront fatigue issues associated with the poor chemical stability of the nanoparticles upon thermal cycling.[4,18] Another limitation comes from the intrinsic insulating character of these SCO nanomaterials, which makes difficult to get an electronic read-out of the spin switching in the device.[21–23] A way to improve the chemical robustness of the SCO NPs consists of protecting them with an inorganic silica (SiO_2) shell. This method was first used by Mallah and co-workers to synthesize SCO [Fe(pyrazine)Pt(CN)$_4$] NPs covered by silica[24] and then extended by Herrera, Colacio and co-workers to wrap the triazole-based coordination polymer [Fe(Htrz)$_2$(trz)](BF$_4$) with the silica shell.[25] These authors used a reverse-micelle procedure to prepare core–shell [Fe(Htrz)$_2$(trz)](BF$_4$)@SiO_2 NPs of *ca.* 100 nm presenting a thick SiO_2 shell of *ca.* 11 nm. A further variation in the synthetic protocol allowed them to reduce the particle size down to 60 nm.[26] These hybrid NPs exhibited improved chemical stability and dispersibility in different solvents, as compared to the bare SCO NPs. In addition, the SiO_2 coating provided an ideal platform for chemical functionalization *via* post-synthetic methods, opening a convenient way to obtain multifunctional NPs. For instance, luminescence or plasmonic properties can be incorporated in these SCO NPs by functionalizing the SiO_2 shell with luminescent molecules or gold (Au) NPs.[27–30]

Despite these attractive features, the presence of a thick SiO_2 shell has a negative effect on the performance of an electronic device based on these NPs. In particular, this insulating shell seriously limits the conductivity through the NPs, making difficult the detection of the spin transition since the switching occurs at very low conductivity levels.[19] To overcome this problem, the synthesis of SCO NPs protected with a thinner SiO_2 shell is mandatory. Thus, this thin shell should be sufficient to enhance the chemical stability of the pristine material, without interfering in the transport properties of the device. In the present work, we report the synthesis of chemically stable Fe-triazole@SiO_2 hybrid NPs presenting different sizes (from *ca.* 90 to 28 nm) and a very thin silica shell (<3 nm).

The general reverse-micelle procedure previously developed to cover SCO NPs with a silica shell consisted of mixing two microemulsions, one containing the Fe salt and the other the triazole ligand. Each one of these micro-emulsions consisted in an organic phase, formed with a non-ionic surfactant (Triton X-100), a co-surfactant (*n*-hexanol) and a hydrocarbon (cyclohexane), with an aqueous phase containing the silica

[a]*Instituto de Ciencia Molecular, Universidad de Valencia, Catedrático José Beltrán 2, 46980 Paterna, Spain. E-mail: monica.gimenez-marques@uv.es, eugenio.coronado@uv.es*
[b]*Kavli Institute of Nanoscience, Delft University of Technology, Lorentzweg 1, 2628 CJ Delft, The Netherlands*

†Electronic supplementary information (ESI) available. See DOI: 10.1039/c9dt02086a

precursor (tetraethyl orthosilicate, TEOS) and the Fe salt or the triazole ligand. In a second step, this mixture was left to react at room temperature. In order to reduce the thickness of this silica shell, we have added the silica precursor (TEOS) in the organic phase, instead of adding it directly in the aqueous phase (see Experimental section, ESI†). We assume that this modification decreases the kinetics of the hydrolysis of the hydrophilic TEOS molecules, which need first to migrate from the organic phase into the aqueous droplets of the micelles, thus resulting in reduced growth of the silica shell.

In order to reduce the size of the SCO core, we have acted on the key parameters involved in the NP nucleation,[10,31,32] namely the reaction time, the surfactant to water ratio (*i.e.*, the ω parameter) and the concentration of Fe(II). Table 1 summarizes how these parameters control the size of the hybrid NPs. As we can notice, two different synthetic scenarios were required: (i) by decreasing reaction time and Fe concentration, a size in the range 90–60 nm was obtained (**1** and **2**, Fig. 1); (ii) by decreasing the ratio between surfactant and water (from ω = 9 to 5) and keeping short reaction times and high Fe concentration, a reduction in the NP size down to a minimum value of 25 nm was achieved (**3** and **4**, Fig. 1). It is important to note that attempts of using ω < 5 resulted in unstable micellar suspensions. The above results could be understood as follows: by increasing the metal concentration in the aqueous phase, the number of nucleation centers increases, leading to a decrease of the NPs final size that can further be reduced by limiting the reaction time during the micellar exchange. On the other hand, a decrease in the ω parameter results in the reduction of the micelle diameter, thus limiting the size of the NP.

Table 1 Correlation between synthetic parameters and the particle size and composition in $[Fe(Htrz)_2(trz)](BF_4)$@SiO_2 NPs

Sample	$[Fe^{2+}]$ (M)	ω	Time (h)	Length (nm)	Width (nm)	Si/Fe
1	1.25	9	24	87 ± 8	49 ± 13	0.7
2	1.5	9	2	60 ± 8	39 ± 8	0.8
3	1.5	8	2	38 ± 7	—	0.8
4	1.5	5	2	28 ± 6	—	1.1

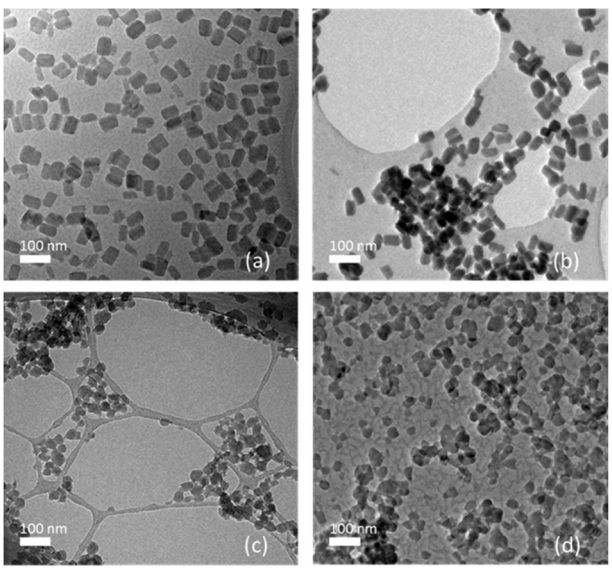

Fig. 1 HR-TEM images of NPs **1** (a), **2** (b), **3** (c) and **4** (d), deposited by drop casting on holey carbon film in (a) and (c), whereas a lacey carbon film was used in (b) and (c).

The stability of these hybrid $[Fe(Htrz)_2(trz)](BF_4)$@SiO_2 NPs has been proved from Dynamic Light Scattering measurements (DLS) in colloidal aqueous suspensions. Essentially, dried samples of NPs **1–4** can be re-dispersed in different solvents including water, maintaining their colloidal and chemical stability up to 3 days. This observation is in sharp contrast with what happens in the pure $[Fe(Htrz)_2(trz)](BF_4)$ NPs coated with organic AOT (AOT = dioctyl sulfosuccinate sodium salt), which are not redispersable once dried in any solvent and rapidly degrade in the form of oxidized species (see Fig. S2†). Therefore, the improved colloidal and chemical stability in the hybrid core@shell NPs is likely provided by the silica shell. DLS measurements performed in these colloidal suspensions afforded hydrodynamic diameter of 137 ± 8 and 68 ± 9 nm for NPs **1** and **2**, and 47 ± 8 and 29 ± 9 nm for NPs **3** and **4** (Fig. S1†). These values are consistent with the more precise values observed by High-Resolution Transmission Electron Microscopy (HR-TEM), which in addition also give information on the morphology and composition of the hybrid NPs. NPs **1–2** present a rod-like morphology with an average side length of 87 ± 8 and 60 ± 8 nm respectively, whereas NPs **3–4** tend to be spherical with a diameter of 38 ± 7 and 28 ± 6 nm, respectively (see Table 1).

To establish the presence of Si, Fe, and O in the NPs, energy-dispersive X-ray spectroscopy (EDS) experiments were performed. Several NPs were mapped for samples **1**, **3**, and **4** for statistical purposes. In all cases, the presence of O and Si at the surface was clearly evidenced (see Fig. S6†). However, the determination of the shell thickness resulted more challenging due to persistent contamination related to the detection limit of the microscope and the shell thickness (close to 1 nm). Only in the case of NPs **1** presenting the largest size, a sharp oxygen shell of *ca.* 3 nm was observed (see Fig. 2a). In

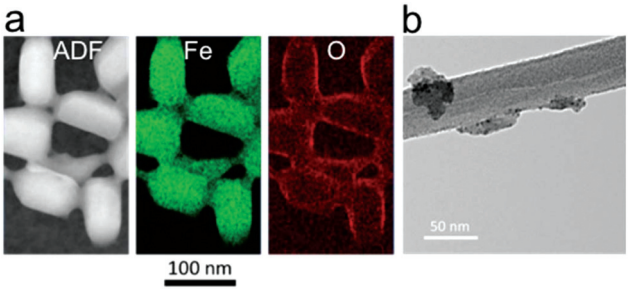

Fig. 2 (a) Annular Dark Field (ADF) STEM image of NPs **1** and EDS maps of Fe and O. (b)HR-TEM image of NPs **4** decorated with Au nanoparticles.

the smaller hybrid NPs (samples **2**, **3** and **4**) the silica shell was indistinguishable from the core.

To proof the presence of a silica coverage in the smallest NPs (sample **4**), we used a chemical approach developed by Li and co-workers,[29] which consists of decorating the silica shell with Au NPs. The Au decoration protocol consisted of the post-functionalization of the silica shell with (3-aminopropyl) triethoxysilane (APTES) to form **4@NH$_2$** NPs. These amino-functionalized NPs were then decorated with $HAuCl_4$ molecules taking advantage of the electrostatic interactions between the $AuCl_4^-$ anions and the amino terminal groups. Finally, the anchored anions were reduced *in situ* to form **4@Au** NPs (Fig. 2b). It is important to note that the original work of Li and co-workers used large SCO NPs of *ca.* 200 nm, whereas in this case the chemical Au decoration is achieved using NPs of *ca.* 28 nm. Fig. 2b reveals the successful decoration of the core–shell NPs **4** with Au NPs of *ca.* 4 nm with a high degree of grafting. Such a directed surface chemistry unequivocally evidences the presence of a thin silica shell and results unsuccessful when pristine SCO NPs are used instead.

The structure and composition of the $[Fe(Htrz)_2(trz)](BF_4)$@SiO_2 hybrid NPs were established by X-ray powder diffraction, inductively coupled plasma optical emission spectrometry (ICP-OES), thermogravimetric analysis (TGA) and Elemental Analysis (EA) (see ESI†). X-ray powder diffraction of the hybrid NPs **1–4** revealed the existence of one single phase corresponding to the simulated pattern of $[Fe(Htrz)_2(trz)](BF_4)$ coordination polymer (see Fig. S3†).[33,34] ICP-OES was used to quantify the amount of Si and Fe after digestion of the NPs under acidic conditions. A molar ratio of Si/Fe comprised between 0.7 and 1.1 was obtained for NPs **1–4**, which represents a two times decrease of Si with respect to the already reported NPs with larger silica shell thickness (see Tables 1, S1 and Fig. S4†).[26] The TGA of the NPs displays the same decomposition temperature than the bulk material,[35] showing that miniaturization does not modify the stability of the compound (Fig. S4†). The molecular formula of the different samples was verified by EA, where the percentage of C, H, and N experimentally obtained is in good agreement with the expected theoretically, $[Fe(Htrz)_2(trz)](BF_4)$, (Table S1†).

Magnetic properties of the Fe-triazole@SiO_2 hybrid NPs were studied in detail. Fig. 3 shows the thermal dependence of the magnetic susceptibility times temperature ($\chi_M T$) for NPs **1–4**, where χ_M is the molar magnetic susceptibility in emu mol^{-1} K. Thermal spin transitions are characterized by the hysteresis width (ΔT) and the corresponding transition temperatures $T_{1/2}^{\uparrow}$ and $T_{1/2}^{\downarrow}$, which are defined as the temperatures for which 50% of both, the LS and HS Fe^{2+} centers are present in the sample for the heating and cooling modes, respectively. All these parameters are summarized in Table 2. $T_{1/2}$ are estimated from the maxima of the $d(\chi_M T)/dT$ curve.

All samples exhibit a characteristic abrupt spin transition centred above room temperature. A subsequent decrease of hysteresis width is observed upon size reduction. A 40% narrowing of the thermal hysteresis is observed, from *ca.* 40 K in NPs **1** ($T_{1/2}^{\uparrow}$ = 376 K and $T_{1/2}^{\downarrow}$ = 339 K) to *ca.* 20 K in NPs **4** ($T_{1/2}^{\uparrow}$ = 364 K and $T_{1/2}^{\downarrow}$ = 342 K). Such a decrease may be related with a drop in the cooperativity of the material and to that observed by some of us in the organic-coated SCO@AOT NPs of the same SCO material.[10] However, it is interesting to note at this point that in these two nanomaterials, the amount of reduction in thermal hysteresis upon downsizing occurs in very different size ranges. Thus, in the organic-coated AOT NPs a narrowing of *ca.* 40% occurs when the particle size is reduced from *ca.* 20 to 4 nm, while in the inorganic-coated NPs this narrowing is observed for a reduction from *ca.* 90 to 28 nm. Essentially, such a different correlation between sizes and reduction in thermal hysteresis may be attributed to the different shell constraint occurring in both the AOT and SiO_2-coated NPs, although the isotropic average size of the coherent crystalline domains in the NPs could also play a role.[36] The HS fraction of the NPs (between 20–40%) is much higher than that found in bulk (*ca.* 10%) and increases as the size of the NPs decreases as expected for the increased ratio of terminal Fe^{II} ions at the surface, which are known to remain in the HS state.

In summary, we have synthesized a family of hybrid $[Fe(Htrz)_2(trz)](BF_4)$@SiO_2 NPs with distinct sizes (from 90 to 28 nm) using an adjusted protocol based on the reverse-micelle technique. In all cases, these SCO NPs are coated by a very thin silica shell (<3 nm), which provides colloidal and chemical stability to the NPs while enabling further surface functionalization and their integration of mechanical or electronic devices. In fact, these NPs have shown to be useful as mechanical actuators over silicon cantilevers,[37] or as active

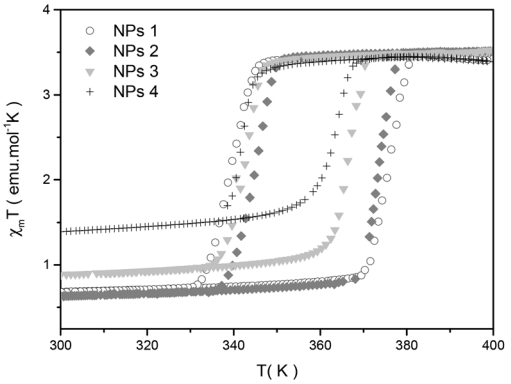

Fig. 3 Comparison of the thermal variation of the $\chi_M T$ product for the different hybrid $[Fe(Htrz)_2(trz)](BF_4)$@SiO_2 NPs **1–4** after several heating–cooling modes.

Table 2 Physical parameters of the thermally induced spin transition for $[Fe(Htrz)_2(trz)](BF_4)$@SiO_2 NPs (**1–4**)

Sample	$T_{1/2}^{\uparrow}$ (K)	$T_{1/2}^{\downarrow}$ (K)	ΔT	HS (%)
1	376	339	37	19
2	373	344	29	18
3	366	342	24	25
4	364	342	22	41

components of nanocomposites based on 2D materials that are sensitive to the stain caused by the spin transition.[38]

Experimental section

Materials

Materials and chemicals. All chemical reagents were purchased and used without further purification. Tetraethyl orthosilicate 98% (Sigma-Aldrich), Triton X-100 (Sigma-Aldrich), ascorbic acid (Sigma-Aldrich), 1,2,4-triazole (Sigma-Aldrich), iron tetrafluoroborate hexahydrate (Sigma-Aldrich), *n*-hexanol (Sigma-Aldrich), cyclohexane (Sigma-Aldrich) and ultra-pure water (18.2 MΩ).

Synthesis

For the synthesis of $[Fe(Htrz)_2(trz)](BF_4)@SiO_2$ NPs of different sizes, we followed the previously reported method by Colacio and Herrera[25,26] with some modifications.

NPs 1. An aqueous solution of $Fe(BF_4)_2{\cdot}6H_2O$ (0.5 mL, 1.25 M) was added to a freshly prepared organic mixture containing Triton X-100 (1.8 mL, ω = 9), *n*-hexanol (1.8 mL), cyclohexane (7.5 mL) and tetraethyl orthosilicate (TEOS) (0.1 mL). The mixture was stirred at room temperature for 15 min to get a stable microemulsion. Then, an aqueous solution of 1,2,4-1*H*-triazole ligand (0.5 mL, 4.5 M) was added to a similarly prepared organic solution containing the TEOS (0.1 mL) and stirred at room temperature for 15 min. Both microemulsions were combined and stirred for 12 h permitting the micellar exchange. NPs were obtained by precipitation upon addition of acetone and collected by centrifugation (12 000 rpm, 10 min), followed by 4 cycles of washing with ethanol and one with acetone to remove the excess of surfactant. Finally, the powdered sample was dried at 70 °C for 2 h.

NP 2. SCO NPs **2** were prepared following the same synthetic procedure as in NP **1** and anticipating the precipitation of the NPs upon addition of acetone after only 2 h of micellar exchange.

NP 3 and 4. The synthesis of NPs **3** and **4** followed the same procedure as in NP 2 but respectively using 2 and 2.7 mL of Triton X.100 (corresponding to ω = 8 and 5, respectively).

NPs 4@NH$_2$. A suspension of 40 mg of NPs 4 in 4.5 mL of ethanol was prepared. Then, 28 μL of (3-aminopropyl)triethoxysilane (APTES) (0.12 mmol) were added dropwise and the mixture was stirred at room temperature for 12 h. The resulting **4@NH$_2$** NPs were washed twice with ethanol (8 mL) and collected by centrifugation (12 000 rpm, 10 min).

NPs 4@Au. An aqueous solution of $HAuCl_4{\cdot}4H_2O$ (3×10^{-3} M, 5 mL) was added into an ethanolic suspension of **4@NH$_2$** NPs (4×10^{-2} M, 20 mL) and stirred for 30 min. Then, $NaBH_4$ (0.1 M, 1.8 mL) solution was added and the mixture was stirred for 5 min. A color change from pink to dark brown after the addition of $NaBH_4$ indicated the formation of the Au NPs. Finally, the gold-decorated NPs were collected by centrifugation (12 000 rpm, 10 min), washed three times with ethanol (8 mL), and then dried at 60 °C in vacuum overnight.

Physical characterization

NPs were characterized by high-resolution transmission electron microscopy (HR-TEM) using a TECNAI G2F20 Ultra-TWIN (200 kV) and a Cs-corrected cubed titan (300 kV) microscope.

Energy-dispersive X-ray spectroscopy (EDS) experiments were performed in Scanning TEM mode (STEM), using an Oxford Instruments X-MaxN 100TLE detector. The elemental maps are produced by collecting an EDX spectrum for each position of the electron beam in the scanned area. This scanned area is selected from an Annular Dark Field (ADF) STEM image. Carbon contamination was excluded or minimized using a MEMS heating device to remove water from the sample. The SiN support film of the MEMS heater was previously removed with etching to enable mapping of NPs suspended above a hole. Sample preparation was done placing a drop of the NPs suspended in a solvent on a carbon coated copper grid obtained from Agar Scientific.

NPs size distributions were determined in suspension by DLS using a Zetasizer ZS (Malvern Instrument, UK) and by "manual counting" of HR-TEM images using ImageJ software.

Phase purity of all samples was established by powder X-ray diffraction (PXRD). Dried samples were lightly ground in an agate mortar and pestle and filled into a 1 mm borosilicate capillary. Data were collected at room temperature on an Empyrean PANalytical powder diffractometer, using Cu Kα radiation (λ = 1.5418 Å) and working on transmission mode.

Fe and Si contents were determined using an inductively coupled plasma mass spectrometry (ICP-MS) Agilent 7900 after the digestion of the powder in acid medium at 180 °C. CHN elemental analyses were carried out in a CE instruments 1110 CHNS elemental analyzer.

Thermogravimetric analysis were carried out by a Mettler Toledo TGA/SDTA 851e model operating in the 25–600 °C range.

Magnetic susceptibility measurements were performed on powdered samples with a Quantum Design MPMS-XL-5 SQUID susceptometer. The susceptibility data were corrected from the diamagnetic contributions and deduced by using Pascal's constant tables. The data were collected in the range 300–400 K upon recording several heating–cooling cycles at a constant rate of 1 K min^{-1} with an applied field of 0.1 T.

Conflicts of interest

The authors declare no conflict of interest.

Acknowledgements

We acknowledge funding from the EU (COST Action MOLSPIN CA15128, ERC Advanced Grant Mol-2D 788222, and RIA action COSMICS 766726), the Spanish MINECO (MAT2017-89993-R) and the Generalitat Valenciana (Prometeo Programme). R. T.-C. and M. G.-M. thank the Spanish MINECO for the FPI and Juan de la Cierva Incorporation fel-

lowships, respectively. M. G.-M. thanks "la Caixa" Foundation for the Junior Leader – Incoming Fellowship 86759. Authors thank the EU support for access to the National Centre for High-Resolution Electron Microscopy in Delft (EC Grant Agreement 312483 – ESTEEM2).

Notes and references

1 P. Gütlich and H. A. Goodwin, *Spin Crossover in Transition Metal Compounds I*, 2004, vol. 1, p. 1.
2 O. Kahn, J. Kröber and C. Jay Martinez, *Adv. Mater.*, 1992, **4**, 718.
3 J. F. Létard, P. Guionneau and L. Goux-Capes, *Spin Crossover Transit. Met. Compd. III*, 2004, vol. 1, p. 221.
4 O. Kahn and C. Jay Martinez, *Science*, 1998, **279**, 44.
5 L. G. Lavrenova, E. V. Kirillova, V. N. Ikorskii, Y. G. Shvedenkov, V. A. Varnek, L. A. Sheludyakova and S. V. Larionov, *Russ. J. Coord. Chem.*, 2001, **27**, 46.
6 O. Roubeau, *Chem. – Eur. J.*, 2012, **18**, 15230.
7 E. Coronado, J. R. Galán-Mascarós, M. Monrabal-Capilla, J. García-Martínez and P. Pardo-Ibáñez, *Adv. Mater.*, 2007, **19**, 1359.
8 T. Forestier, A. Kaiba, S. Pechev, D. Denux, P. Guionneau, C. Etrillard, N. Daro, E. Freysz and J. F. Létard, *Chem. – Eur. J.*, 2009, **15**, 6122.
9 J. R. Galán-Mascarós, E. Coronado, A. Forment-Aliaga, M. Monrabal-Capilla, E. Pinilla-Cienfuegos and M. Ceolin, *Inorg. Chem.*, 2010, **49**, 5706.
10 M. Giménez-Marqués, M. L. García-Sanz de Larrea and E. Coronado, *J. Mater. Chem. C*, 2015, **3**, 7946.
11 F. Volatron, L. Catala, E. Rivière, A. Gloter, O. Stéphan and T. Mallah, *Inorg. Chem.*, 2008, **47**, 6584.
12 C. Bartual-Murgui, A. Cerf, C. Thibault, C. Vieu, L. Salmon, G. Molnár and A. Bousseksou, *Microelectron. Eng.*, 2013, **111**, 365.
13 I. A. Gural'skiy, C. M. Quintero, G. Molnár, I. O. Fritsky, L. Salmon and A. Bousseksou, *Chem. – Eur. J.*, 2012, **18**, 9946.
14 I. A. Gural'skiy, G. Molnár, I. O. Fritsky, L. Salmon and A. Bousseksou, *Polyhedron*, 2012, **38**, 245.
15 J. Dugay, M. Giménez-Marqués, T. Kozlova, H. W. Zandbergen, E. Coronado and H. S. J. van der Zant, *Adv. Mater.*, 2015, **27**, 1288.
16 A. Rotaru, J. Dugay, R. P. Tan, I. A. Guralskiy, L. Salmon, P. Demont, J. Carrey, G. Molnár, M. Respaud and A. Bousseksou, *Adv. Mater.*, 2013, **25**, 1745.
17 (*a*) A. Rotaru, I. a. Gural'skiy, G. Molnár, L. Salmon, P. Demont and A. Bousseksou, *Chem. Commun.*, 2012, **48**, 4163; (*b*) J. Dugay, W. Evers, R. Torres-Cavanillas, M. Giménez-Marqués, E. Coronado and H. S. Van der Zant, *J. Phys. Chem. Lett.*, 2018, **9**(19), 5672.
18 F. Prins, M. Monrabal-Capilla, E. A. Osorio, E. Coronado and H. S. J. Van Der Zant, *Adv. Mater.*, 2011, **23**, 1545.
19 A. Holovchenko, J. Dugay, M. Giménez-Marqués, R. Torres-Cavanillas, E. Coronado and H. S. J. van der Zant, *Adv. Mater.*, 2016, **28**, 7228.
20 J. Dugay, M. Aarts, M. Giménez-Marqués, T. Kozlova, H. W. Zandbergen, E. Coronado and H. S. J. Van Der Zant, *Nano Lett.*, 2017, **17**, 186.
21 C. Lefter, R. Tan, J. Dugay, S. Tricard, G. Molnár, L. Salmon, J. Carrey, A. Rotaru and A. Bousseksou, *Phys. Chem. Chem. Phys.*, 2015, **17**, 5151.
22 C. Lefter, R. Tan, S. Tricard, J. Dugay, G. Molnár, L. Salmon, J. Carrey, A. Rotaru and A. Bousseksou, *Polyhedron*, 2015, **102**, 434.
23 (*a*) C. Lefter, R. Tan, J. Dugay, S. Tricard, G. Molnár, L. Salmon, J. Carrey, W. Nicolazzi, A. Rotaru and A. Bousseksou, *Chem. Phys. Lett.*, 2016, **644**, 138; (*b*) R. Torres-Cavanillas, R. Sanchis-Gual, J. Dugay, M. Coronado-Puchau, M. Giménez-Marqués and E. Coronado, *Adv. Mater.*, 2019, 1900039.
24 Y. Raza, F. Volatron, S. Moldovan, O. Ersen, V. Huc, C. Martini, F. Brisset, A. Gloter, O. Stéphan, A. Bousseksou, L. Catala and T. Mallah, *Chem. Commun.*, 2011, **47**, 11501.
25 S. Titos-Padilla, J. M. Herrera, X.-W. Chen, J. J. Delgado and E. Colacio, *Angew. Chem.*, 2011, **123**, 3348.
26 J. M. Herrera, S. Titos-Padilla, S. J. a. Pope, I. Berlanga, F. Zamora, J. J. Delgado, K. V. Kamenev, X. Wang, A. Prescimone, E. K. Brechin and E. Colacio, *J. Mater. Chem. C*, 2015, **3**, 7819.
27 Y. a. Tobon, C. Etrillard, O. Nguyen, J.-F. Létard, V. Faramarzi, J. F. Dayen, B. Doudin, D. M. Bassani and F. Guillaume, *Eur. J. Inorg. Chem.*, 2012, 5837.
28 L. Moulet, N. Daro, S. Mornet, N. Vilar-Vidal, G. Chastanet and P. Guionneau, *Chem. Commun.*, 2016, **52**, 13213.
29 D. Qiu, L. Gu, X.-L. Sun, D.-H. Ren, Z.-G. Gu and Z. Li, *RSC Adv.*, 2014, **4**, 61313.
30 I. Suleimanov, J. Sánchez Costa, G. Molnár, L. Salmon and A. Bousseksou, *Chem. Commun.*, 2014, **50**, 13015.
31 M. P. Pileni, *Adv. Colloid Interface Sci.*, 1993, **46**, 139.
32 L. Moulet, N. Daro, C. Etrillard, J.-F. Létard, A. Grosjean and P. Guionneau, *Magnetochemistry*, 2016, **2**, 10.
33 A. Grosjean, N. Daro, B. Kauffmann, A. Kaiba, J.-F. Létard and P. Guionneau, *Chem. Commun.*, 2011, **47**, 12382.
34 A. Urakawa, W. Van Beek, M. Monrabal-Capilla, J. R. Galán-Mascarós, L. Palin and M. Milanesio, *J. Phys. Chem. C*, 2011, **115**, 1323.
35 C. Faulmann, J. Chahine, I. Malfant, D. de Caro, B. Cormary and L. Valade, *Dalton Trans.*, 2011, **40**(11), 2480.
36 A. Grosjean, N. Daro, S. Pechev, C. Etrillard, G. Chastanet and P. Guionneau, *Eur. J. Inorg. Chem.*, 2018, 429.
37 J. Dugay, M. Giménez-Marqués, W. J. Venstra, R. Torres-Cavanillas, U. N. Sheombarsing, N. Manca, E. Coronado and H. S. J. van der Zant, *Phys. Chem. C*, 2019, **123**(11), 6778.
38 R. Torres-Cavanillas, M. Morant-Giner, G. Escorcia, M. Galbiati, S. Tatay, J. Dugay, M. Giménez-Marqués, A. Forment-Aliaga and E. Coronado, paper in preparation.